Noname manuscript No.
(will be inserted by the editor)

Normal Shock Wave Attenuation During Propagation in Ducts with Grooves

Seyed Mehdi Mortazawy · Konstantinos Kontis · John Ekaterinaris

Received: date / Accepted: date

Abstract Experimental investigations and numerical simulations of normal shock waves of different strengths propagating inside ducts with roughness are presented. The roughness is added in the form of grooves. Straight and branching ducts are considered in order to better explore the mechanisms causing attenuation of the shock and the physics behind the evolution of the complex wave patterns resulting from diffraction and reflection of the primary moving shock. A well-established finite volume numerical method is used and further validated for several test cases relevant to this study. The computed results are compared with experimental measurements in ducts with grooves. Good agreement between high-resolution simulations and the experiment is obtained for the shock speeds and complex wave patterns created by the grooves. High frequency response time histories of pressure at various locations were recorded in the experiments. The recorded pressure histories and shock strengths were found in fair agreement with the two-dimensional simulation results as long as the shock stays in the duct. Overall, the physics of the interactions of the moving shock, and the diffracted and reflected waves with the grooves are adequately captured in the high-resolution simulations. Therefore, shocks propagating in ducts with different groove geometries have been simulated in order to identify the groove shape that diminishes shock strength.

Keywords Moving shock wave · shock diffraction · shock reflection · shock attenuation · shock–vortex interaction · pressure wave–vortex interaction.

Mehdi Mortazawy
Department of Aerospace Engineering, Embry-Riddle Aeronautical University, 600 S Clyde Morris Blvd, Daytona Beach, FL 32114
Tel.: +1(386)-882-1435
E-mail: mortazas@my.erau.edu

Konstantinos Kontis
School of Engineering, University of Glasgow, James Watt South Building, Glasgow, G12 8qq
Tel.: +01413304337
E-mail: kostas.kontis@glasgow.ac.uk

John Ekaterinaris
Department of Aerospace Engineering, Embry-Riddle Aeronautical University, 600 S Clyde Morris Blvd, Daytona Beach, FL 32114
Tel.: +1(386)-226-6100
E-mail: ekaterij@erau.edu

1 Introduction

Investigation of complex shock interactions for external and internal flows has been an area of continuous interest. It was found that for certain high-speed flows, the viscous flow effects are not very significant and time accurate high-resolution numerical solutions of the inviscid flow equations (Euler equations) were in excellent agreement with the experiment [1–6]. In other cases however, viscous flow effects were found to be significant [7–9], and the numerical solution of the full compressible Navier-Stokes equations was required.

In many applications, unsteady shock wave interaction with boundary layers and the strong pressure waves following moving shock interactions with non-smooth geometries are some of the primary causes of performance degradation, structural fatigue, and reduction in air intake efficiency. For example, shock wave–boundary layer interaction, shock–vortex interaction, and unsteady vortex shedding are major contributors to intense broadband noise [10]. Highly unsteady turbulent flow develops behind the moving normal shock, however, the large extend of the domain does not allow to perform high fidelity LES or DNS even for a portion

of the test section. It will be demonstrated that even three-dimensional unsteady Reynolds averaged Navier-Stokes (RANS) or URANS high-resolution simulations for the full domain of the experiment, so that the shocks captured within two or three cells are confined in a reasonably narrow region, are beyond the available computing resources.

Pressure attenuation of a moving shock propagating in a duct encompasses the phenomena mentioned above and it is of importance in a wide variety of applications such as health and safety, transportation (high-speed trains and car silencers), and the chemical industry (pipe loading). Propagation of shock waves from explosions in tunnels create damage and may result in loss of lives. Attenuation of shocks in mines and tunnels for example is of great importance to safety. The pressure waves that are generated by diffraction and refraction and follow the propagating shock, after a lapse of time merge, become stronger and often can form new shock waves [11]. Pressure attenuation of shock waves is inherently present in exhaust ducts and tunnels, where the roughness of the walls play an important role in the pressure attenuation upstream. Previous studies [4] have shown that shock wave strength tends to decay faster when it propagates into a branched duct or into large damping chambers, where the main mechanism responsible for weakening the shock wave is several expansion waves caused by the grooves and the branched ducts. On the other hand, it was observed that amplification of strong pressure waves often occurs due to multiple reflections or compression waves and leads to development of secondary shocks.

Several experimental and numerical investigations have shown that increasing the roughness on the wall of a duct or tunnel can suppress the pressure jump of a propagating shock [4, 6]. One way to achieve this is by incorporating groves on the wall which causes pressure and noise suppression through multiple reflection and expansion of the primary incident shock. However, there is no evidence of a systematic study for a shock wave propagation in a closed duct that is directly extended from the driven section of a shock tube. Most of the previous works have evolved around studying an external explosive type shock wave that enters a duct from outside, hence very little or almost no development of boundary layer and viscous effects. Direct simulation of three-dimensional turbulent flow following propagating shocks in complex geometries [4] is, however, not possible for the present experiment, and numerical studies complementing the experiments are based on the URANS simulation and they are mostly two-dimensional.

The objective of this investigation is to study a moving normal shock in a square duct with grooves through combined experimental studies and numerical simulations. The numerical simulations are for the same geometry of the experimental test section and suitably chosen inflow conditions of a series of experiments carried out at the high-speed experimental facilities of the University of Manchester [12, 13]. The objective of the experiment was to identify the effect of grooves on the attenuation and alteration of a shock wave propagating through a square duct. It is shown that three-dimensional effects due to the square duct section have small effect on wave patterns in the core region. As a result, high-resolution two-dimensional simulation in a channel-like geometry representing the duct with plane side walls may be used to gain further insight of the complex flow phenomena following the passage of the shock over the grooves. In the experiments, the shape of the grooves remained fixed while different wall junction angles were considered. For these arrangements, attenuation of shock with varying strengths was also investigated.

Overall, good agreement of the experiment and the two-dimensional simulations was achieved during the time the shock remains in the square duct and three-dimensionality of the flow has smaller effect. As a result, confidence was gained that the high-resolution simulations capture the main flow physics of the interaction of the moving shock with the grooves. Therefore, different groove geometries have been tested in the numerical simulation in order to identify the shape that will better diminish shock strength. Furthermore, analysis of instantaneous realizations and animations of the computed results have been employed to reveal salient features of the unsteady flow field. Some of the intended applications of these experimental investigations are escape of exhaust gases from car engine through silencers (mufflers), high-speed trains passing through a tunnel, explosions in mines, tunnels, and confined buildings, where the compression waves travel through ventilation systems which in turn has great impacts on health and safety.

The rest of this paper is organized as follows. The experimental setup is presented first, and some representative measurements are shown. The numerical methodology and some essential features of the algorithm are presented next. Demonstration of the resolving ability of the numerical method employed in the simulations is carried out for relevant test cases. These validation cases are shown along with a preliminary numerical study for the groove geometry used in the experiment. Finally, experimental findings and comparisons with simulations are presented.

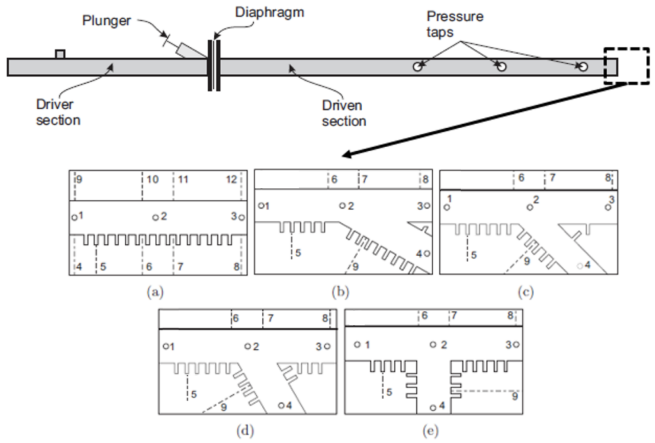

Fig. 1: Schematic of the shock tube with test section configurations; (a) 0°, (b) 30°, (c) 45°, (d) 60°, and (e) 90° junctions [12]

2 Experimental Setup

A comprehensive study of a moving normal shock wave interacting with grooves inside the test section of a square duct was conducted at the University of Manchester [12, 13]. The cross sectional area of the shock tube was: 25 mm × 25 mm. Three pressure ratios: P_L/P_R = 4, 8, and 12 across the shock tube diaphragm were considered. Straight tube geometries with grooves and a range of branching tubes with junction angles of up to 150°(see Fig. 1) were used for a test section, which resulted in a total of 24 configurations. The test section was placed at the end of the driven section of the shock tube. The length of the driver, driven, and the test section are: 700 mm, 1750 mm, and 130 mm, respectively. Roughness was introduced only inside the test section in the form of grooves either on the bottom side or both top and bottom sides in order to evaluate shock attenuation. The grooves dimensions are: 2.5 mm wide and 7.5 mm deep with 5 mm spacing between each one. Pressure transducers were placed at several locations inside the test section to record the variation of pressure during the passage of the shock. Furthermore, the interaction of the shock with the grooves and the resulting complex wave patterns were recorded using high-speed schlieren photography. The schematic of the shock tube and some of the test section configurations are depicted in Fig. 1, where P_{L} denotes the initial driver pressure, while P_{R} is the initial driven pressure on the right side. The transducer T_5 is located at the bottom wall of the second groove, where it indicates the accumulation of pressure on the grooves and the slow release of the stored energy for all pressure ratios. After the diaphragm ruptures, the propagating shock speed in still gas and the mass flow speed behind it are denoted by W_{S} and u_{p}, respectively. The theoretical Mach number of the moving shock wave M_{S} is a function of the pressure ratio across the diaphragm $(P_{\mathrm{L}}/P_{\mathrm{R}})$ [14], and for air as the selected gas, is given by Eq. 1, where γ is the specific heat ratio, and a represents the speed of sound.

$$\frac{P_{\mathrm{L}}}{P_{\mathrm{R}}} = \frac{2\gamma M_{\mathrm{S}}^2 - (\gamma - 1)}{(\gamma + 1)} \left[1 - \frac{\gamma - 1}{\gamma + 1} \cdot \frac{a_{\mathrm{L}}}{a_{\mathrm{R}}} \left(M_{\mathrm{S}} - \frac{1}{M_{\mathrm{S}}}\right)\right]^{-\frac{2\gamma}{\gamma - 1}} \quad (1)$$

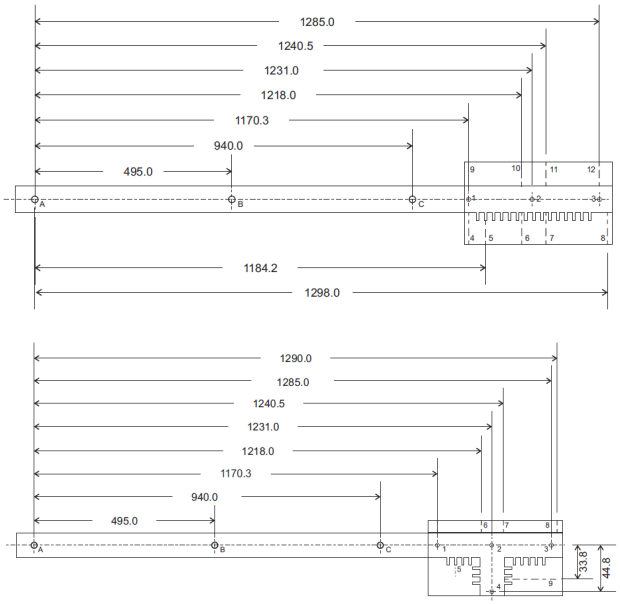

Fig. 2: Location of transducers for 0° and 90° pipe for solid-groove and groove-groove configuration (dimensions in mm) [12]

Table 1 shows the flow properties corresponding to each diaphragm pressure ratio $(P_{\mathrm{L}}/P_{\mathrm{R}})$, where $*$ represents the condition across the right-moving shock and u_{p} is the induced mass flow speed behind the moving shock. These parameters are sufficient to reproduce and extend the shock tube simulation in future. The shock speed obtained from Eq. 1 and the shock speed deduced from the travelling shock wave Mach number from pulses emanating from two pressure gauges located a known distance from each other were found the same.

Table 1: Theoretical flow properties of the moving shock

$P_{\mathrm{L}}/P_{\mathrm{R}}$	$P_{\mathrm{L}}/P_{\mathrm{R}_*}$	$\rho_{\mathrm{L}}/\rho_{\mathrm{R}_*}$	$u_{\mathrm{p}}(m/s)$	M_{S}
4	1.928	1.585	168.4	1.34
8	2.599	1.929	252.4	1.54
12	3.064	2.138	301.5	1.66

Drawings of the test sections used for constructing the computational domain in the numerical simulation for the straight and the 90° branched duct with grooves on one-side are shown in Fig. 2.

In addition to the straight duct, the branched angles of the junction were varied in the range of 30° to 150°. The experiments were performed with the pressure in the driven section being ambient. The grooves give rise to a series of compression and expansion waves when the incident shock wave propagates over them as shown in the schematic of Fig. 3. The diffracted (D) and re-

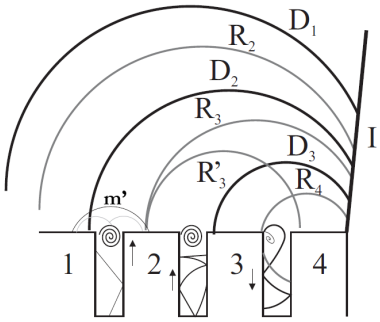

Fig. 3: Schematic of behaviour of transmitted waves inside grooves [12]

flected (R) waves are indicated with the corresponding groove number. The side walls of the square duct are smooth, and these compression and expansion waves propagate radially. Therefore, the influence of the waves is seen upstream in the flow field following the normal shock. The reduction of the velocity on the shock front when encountering the grooves is due to the expansion waves propagating upstream. The diffraction of the incident normal shock wave occurs when it reaches the junctions which also contributes to the deceleration of the shock front. The compression waves which exit the grooves (m') on the walls after a period of time are responsible for the pressure increase upstream. Additionally, coalescence of the compression waves forms a secondary moving shock wave propagating downstream behind the primary normal shock front. A secondary normal shock forms when the double-groove configuration is used for the test section wall. Sample schlieren snapshots in branching ducts, along with the corresponding pressure history and shock speed plots from the experiment, are shown in Figs. 4 and 5. Additional cases for straight and branching ducts are presented in more detail in the following sections and comparisons with numerical simulations are shown. The shock speeds extracted from the measurements are shown in Fig. 5 (left), and the legend corresponds to different bifurcation angles. For the recorded pressure histories of Fig. 5 (right), SG and G correspond to the single-groove and double-groove wall configurations, respectively, with the subscripts referring to the pressure ratio across the diaphragm (P_L/P_R).

The recorded pressure histories are for a time longer than the time required for the shock to traverse the domain. Once the shock exits from the square duct, three-dimensional effects become more pronounced and the computational domain must be significantly extended, even for two-dimensional simulations in order to avoid development of nonphysical reflected spurious waves from the end of the domain.

3 Computational Approach

The simulations were carried out using the state-of-the-art open-source SU^2 code [15], which has been developed at Stanford University, and is continuously improving with the addition of new features. It is based on the finite-volume method for unstructured meshes and has been extensively validated and used for large scale simulations. Some modifications are made in the SU^2 code version 5.0 Raven in order to simulate moving shock waves. For all numerical computations, the Harten-Lax-van Leer-contact (HLLC) numerical flux [16] has been employed. Time marching for all cases considered is performed using second-order accuracy and dual time stepping, in order to achieve a time accurate solution with relatively large time steps while still providing sufficient resolution in time of the physical phenomena of interest. The SU^2 code is second-order accurate in space and requires very fine meshes to achieve high resolution and accurate capturing of shock waves, the strong pressure waves, and the small vortices (see Fig. 3) with little diffusion, and within a narrow region. Therefore very small cell size, less than 1/50 of the groove width, must be employed taking into account that the size of the grooves in the present experiment is small.

Previous numerical simulations of high-speed flows with shocks have employed high order methods, such as fifth-order accurate in space or higher Weighted Essentially Non-Oscillatory (WENO) schemes [10, 17], or the Discontinuous Galerkin (DG) method [18]. High order methods for viscous flows however are computationally intensive. The SU^2 code has adaptive mesh refinement capabilities. It was found that for simpler shock interactions, adaptive mesh refinement (h-refinement) can yield superior resolution [18]. The unsteady complex wave interactions of the present study (see Fig. 4 for example), show that almost the entire domain of interest must be adapted; therefore in this work an adaptive mesh refinement strategy was not adopted. Application of h/p-refinement [19] is more suitable for unsteady complex wave interactions however p-type refinement capabilities are possible for finite-element methods, and are not currently available in the SU^2 code since DG capabilities are still under development.

4 Validation and Preliminary Test

4.1 Classical Validation and Test Cases

Further validation of the numerical method and the particular schemes of the SU^2 code (the HLLC numerical flux, and dual time-stepping temporal method) used

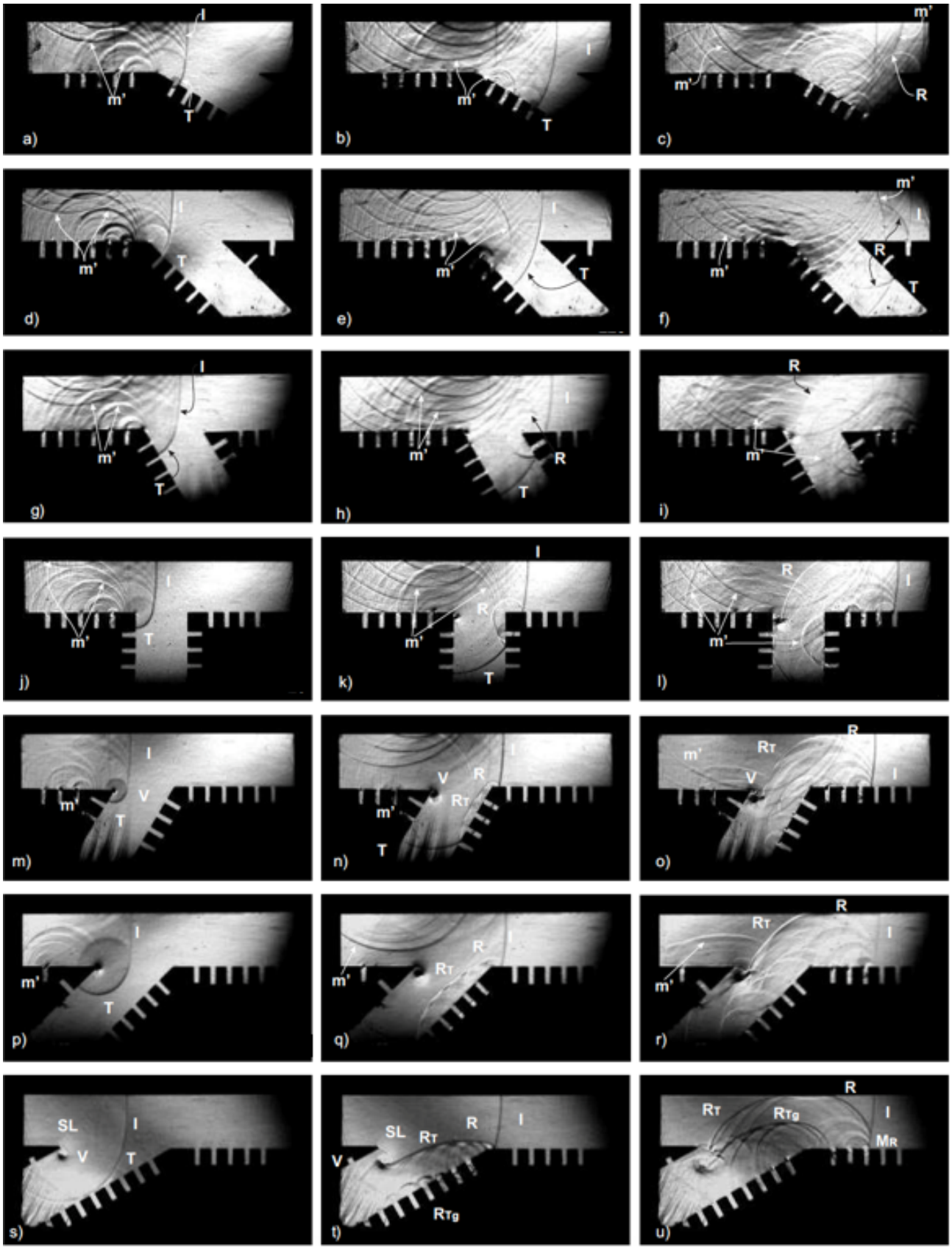

Fig. 4: Experimental schlieren [12] for different junction angles (From top: 30°, 45°, 60°, 90°, 120°, 135°, 150°) with $P_{\mathrm{L}}/P_{\mathrm{R}} = 4$.

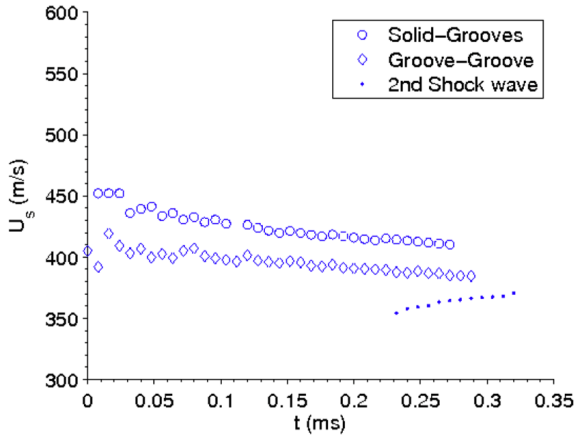

(a)

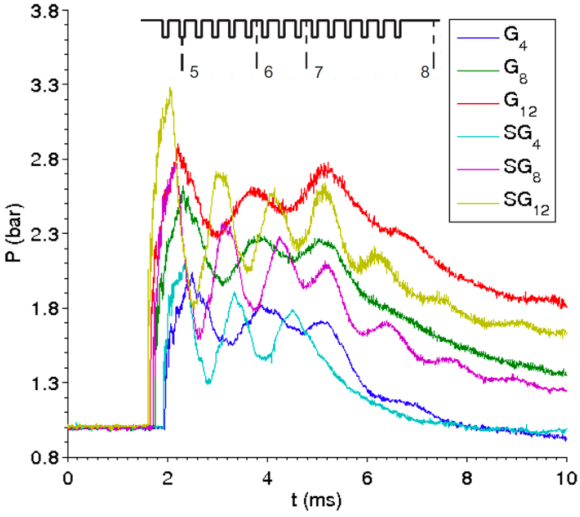

(b)

Fig. 5: (a) Experimental shock speed for $P_L/P_R = 4$, (b) Pressure history at pressure probe T_8 for various shock strengths: $P_L/P_R = 4, 8, 12$. Obtained from [12].

for the simulation was carried out first for several classical test cases of relevance to the present work. A high-resolution simulation was performed for a shock tube and the comparison with the exact solution (not shown here) for the Sod's shock tube problem showed excellent agreement. It was found that for the resolution of the shock, the HLLC numerical flux had better performance compared to the Lax-Friedrichs (LF) or Roe flux for example. Therefore the HLLC numerical flux was used for all the simulations of the current study. Another test case relevant to the features encountered in this study is the shock diffraction over a backward-facing step which was studied in the past [20, 21]. A validation for this test case as it relates to the present simulations is shown in the Fig. 6. It appears that even the inviscid two-dimensional flow simulation is capable

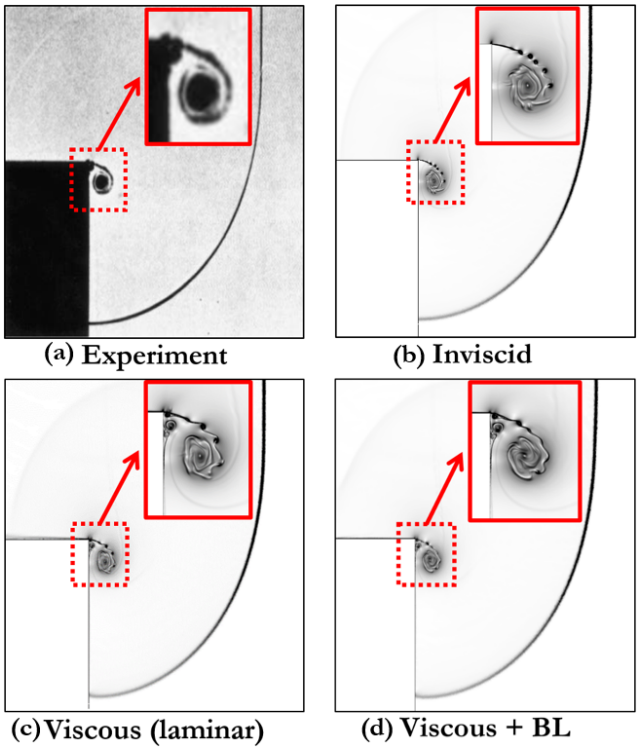

Fig. 6: Comparison of experiment with the SU^2 simulation of a weak shock ($M_S = 1.34$) diffraction.

of capturing a vortex at the corner. However, viscous flow effects appear to be important even at early stages and only the laminar flow simulation is capable of capturing a secondary vortex as in the experiment. In the experiment of Fig. 6 (a), right after the passage of the shock over the wall the near-wall viscous flow effects are negligible since only a thin viscous layer has been developed. In the simulation of Fig. 6 (d) at certain distance upstream of the shock, a laminar boundary layer following the shock was added. The simulation of a shock followed by a wall shear flow shows that small different effects become apparent at the roll-ups of the shear layer. It will be discussed later that near wall developing flow appears to affect the flow structures in the grooves.

4.2 Preliminary Test: Shock Propagating over Grooves

As a preliminary test, the propagation and diffraction of a shock over two consecutive grooves with geometry identical to those of the experiment has been considered. The Mach number of the moving normal shock is $M_S = 1.34$, corresponding to a pressure ratio of $P_L/P_R = 4$, which is the same as that studied in the experiment [12, 13]. The pressure and temperature on the right side is atmospheric $P_R = 101325$ Pa and

$T_R = 300$ K. It was shown before that viscous flow effects become important (see Fig. 6) even at early stages of shock diffraction. For the sake of comparison, in the present case where the shock diffracts over the first two grooves only, both Euler and Navier-Stokes laminar flow simulations are obtained and the results are compared. These simulations were performed with a very-high-resolution mesh with the objective to study features of the flow that are otherwise not visible in the experiment but they are closely associated with the recorded pressure variation as seen in Fig. 5b for example.

The simulations were run up to double the duration it takes for the shock to move from left to right completely, which is approximately $t_{total} \approx 0.14$ ms. Numerical schlieren of the inviscid and viscous flow simulations at two different times are shown in Figs. 7a and 7b along with links to animation of the flow shown in the caption. For viscous flow, both a sharp and a rounded groove geometry have been considered. In Fig. 7a the diffracted shock is reaching the bottom of the first groove, while in Fig. 7b the reflected shock is passing through the main vortex in the first groove. The slowdown of the shock at its foot is clearly visible in Fig. 7a. In Fig. 7a, a stronger reflection of the shock is seen in the round groove compared to the sharp groove due to the round geometry at the top right edge of the first groove. This reflection is seen to directly affect the primary moving shock front as seen at $x = 14$ mm. In addition, formation of secondary vortex is seen in the viscous flow simulation compared to the inviscid solution, as it has been also shown for the shock diffraction problem. At the later time shown in Fig. 7b, stronger refraction of the shock above the first groove is seen for the round case compared to the sharp case (around $y = -12$ mm. Also, smaller and more concentrated vortices are seen next to the top left corner of the first groove (around $x = 5$ mm for the round edge compared to the sharp case. The consecutive reflections in the grooves and the interactions of shocks and pressure waves with the vortices forming at the corners causes small scale oscillations on the surface pressure that are captured both in the high frequency response experimental measurements and the numerical simulations. All these processes can be clearly observed in the animations.

After demonstrating that shock propagation and complex shock interactions can be computed accurately using several test cases, and the preliminary test with two grooves, two-dimensional inviscid flow simulations of the experimental test section only for straight ducts was performed. A diaphragm pressure ratio of: $P_L/P_R = 4$ has been used in the duct with grooves either on one side (bottom, or both sides (top and bottom) to demonstrate the effect of higher shock strength. The results are compared against those of the experiment qualitatively in Fig. 8 for the shock patterns of schlieren, and quantitatively in Fig. 9 for pressure history of the pressure probes T_5 and T_8 (see Fig. 1) for the one-sided grooves only.

In the comparisons, the theoretical Mach number of the moving shock is $M_S = 1.34$ corresponding to a pressure ratio of $P_L/P_R = 4$. The pressure and temperature on the right side is atmospheric $P_R = 101325$ Pa and $T_R = 300$ K. It was confirmed through running several additional simulations that the results of the previous cases are independent of mesh type; whether structured-like (quadrilateral) or unstructured (triangular), while maintaining the same grid density and cell size. Therefore, a uniform unstructured mesh was used for simulating the experiment in order to facilitate demonstration of a grid independent numerical solution. A grid dependence study was performed for a coarse, a medium, and a fine mesh for the straight duct with single-sided grooves, using inviscid flow simulations. The following mesh sequence was employed: a very coarse mesh with $\Delta h = 0.9$, a medium mesh with $\Delta h = 0.1$, and a fine mesh with $\Delta h = 0.05$, resulting in a total cell size of 0.2, 1.8, and 6.5 million cells, respectively.

Comparison of numerical schlieren of the inviscid simulations for the single-sided grooves even for the medium grid, with the experimental schlieren are favourable and they are presented in Fig. 8 (Top) (Online Resource 4) at two different times. For each configuration a link to the animation is provided in the caption. The flow pattern in the grooves shown in Fig. 8 becomes progressively more complex compared to the pattern shown in Fig. 7a as the shock is advancing over more grooves but it is still well resolved. Due to the non-symmetric geometry (single-sided grooves), the coalescence of the compression waves form an oblique shock behind the primary shock. According to a previous study [22], the distance between the compression waves emerging from the grooves and the primary moving shock wave is determined by the strength of the moving shock (M_S), the depth (h) and the width (w) of the grooves, and the spacing between the grooves, which in this case are: $M_S = 1.34$, $h = 7.5$ mm, $w = 2.5$ mm, and $d = 5$ mm, respectively. For better clarity, a zoomed view of the region behind the primary moving shock is also provided in Fig. 8. Detailed transient behaviour of the vortex and shock reflections inside each groove can be seen from the high-resolution computations. The results for the double-sided grooved duct are also shown in Fig. 8 (Bottom) (Online Resource 5). The results are in favourable

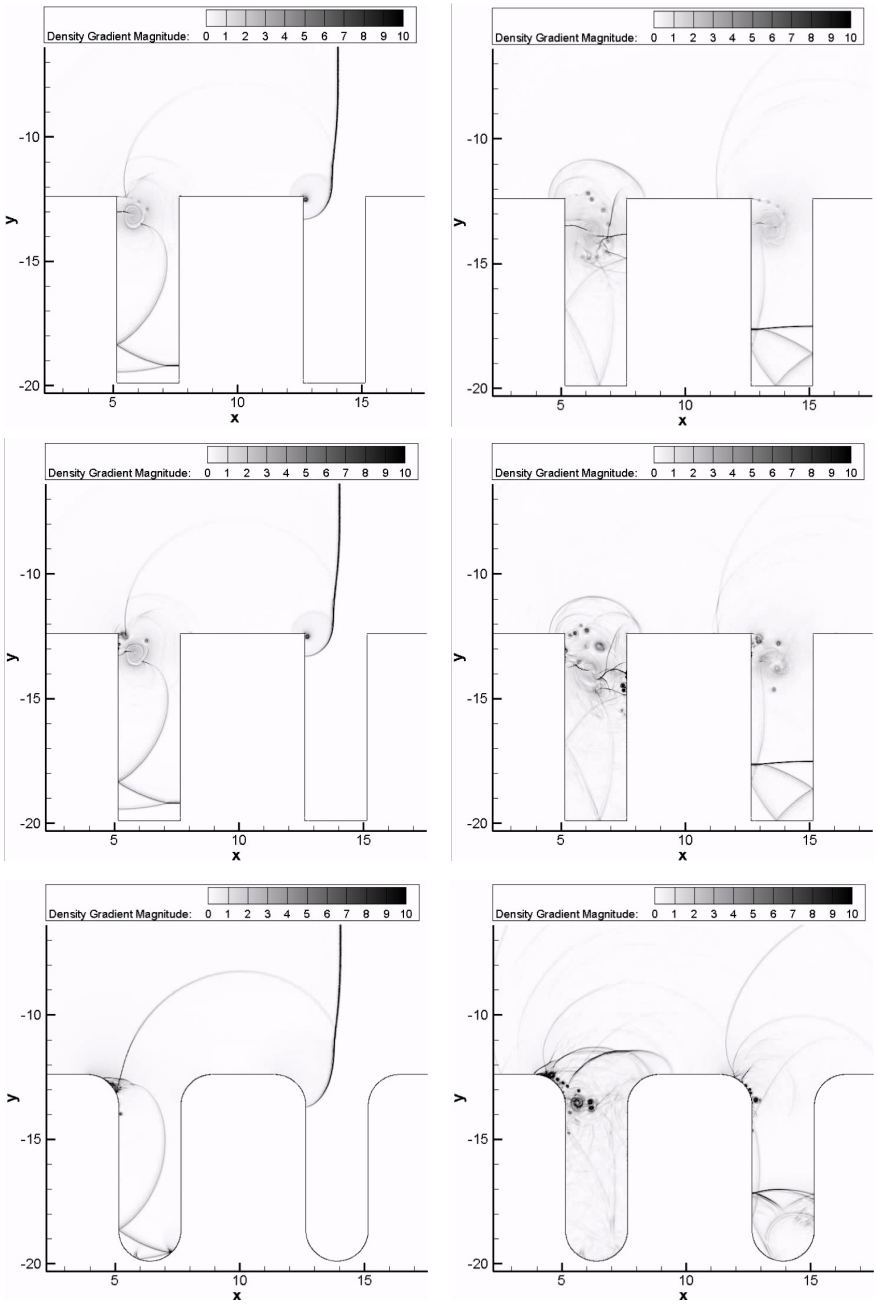

(a) $t = 30$ μs (b) $t = 60$ μs

Fig. 7: Numerical schlieren. From top to bottom: inviscid (Online Resource 1), viscous (Online Resource 2), viscous (Online Resource 3).

qualitative agreement with the experiment. Due to symmetry of the geometry (grooves at the top and bottom) and coalescence of the symmetric compression waves, a secondary moving normal shock is eventually formed behind the primary incident shock. Detailed transient behaviour of the vortex and shock reflections inside each groove can be clearly seen from the simulations.

It was demonstrated already that viscous flow effects alter the near wall flow structure significantly. In order to further demonstrate the importance of viscous flow effects, the time history of pressure predicted from inviscid flow simulation for two locations along the bottom side of the duct are shown for all mesh sizes and compared with the experiment in Fig. 9. The results are shown up until the shock has exited from the square

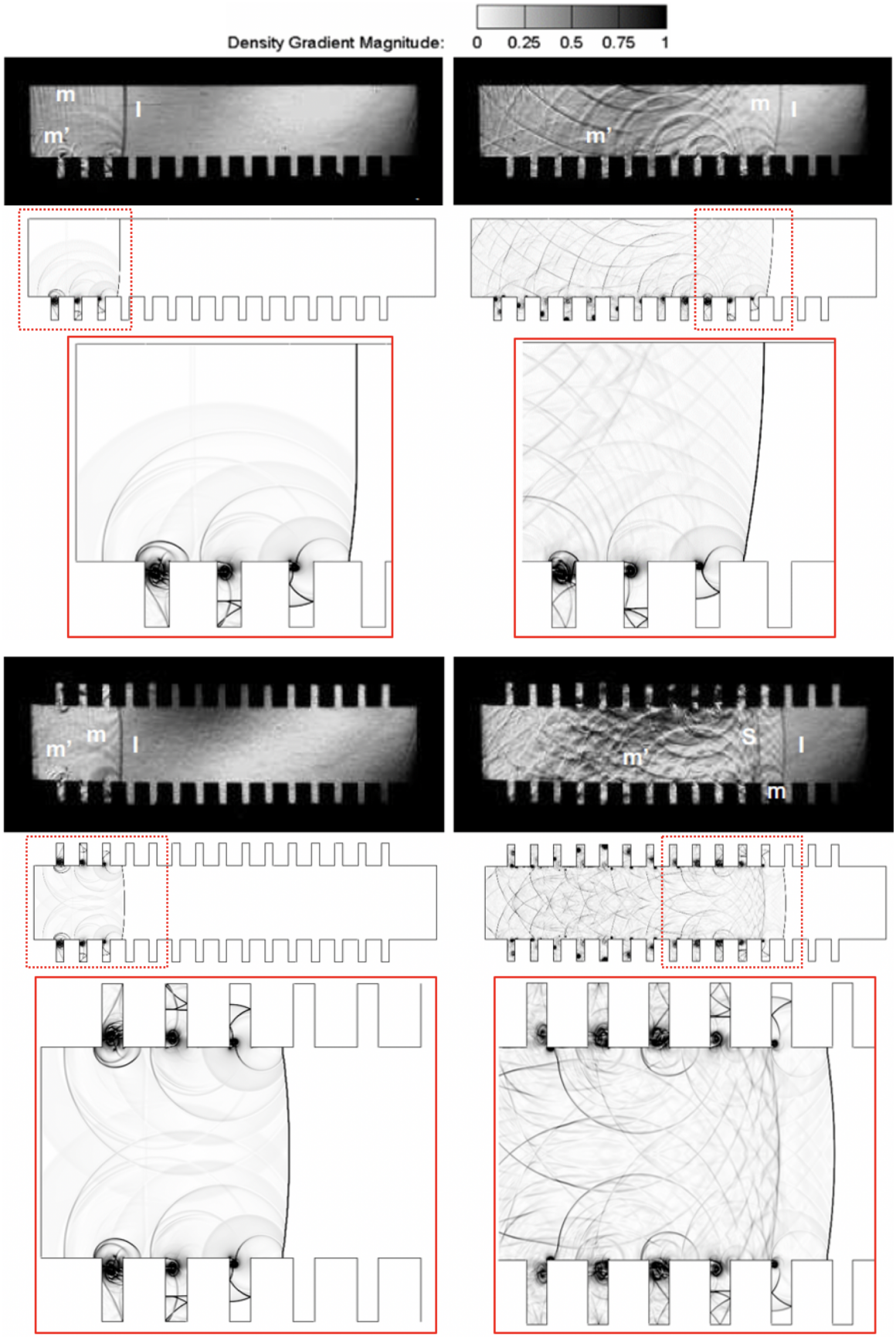

Fig. 8: Comparison of experimental and numerical schlieren for a right-moving shock of $M_S = 1.34$ ($P_L/P_R = 4$) inside (Top): single-sided (Online Resource 4), and (Bottom): double-sided (Online Resource 5) grooved duct.

duct with 100 mm extension after the test section. The general trends of the pressure in terms of peaks and valleys are captured. It can also be seen that medium and fine mesh simulations appear to have reached grid independent solutions. Higher frequency oscillations that are caused by vortex pressure wave interactions evident also in the experiment are captured only in the medium and fine resolution grid. The highest peak is found at pressure probe T_5 which agrees with shock reflection theory. Phase errors can also be seen past $t = 210$ μs. It is interesting to note that at the pressure probe T_8 the main flow features (peaks and valleys) are captured by all grids even though the peaks and valleys have different values.

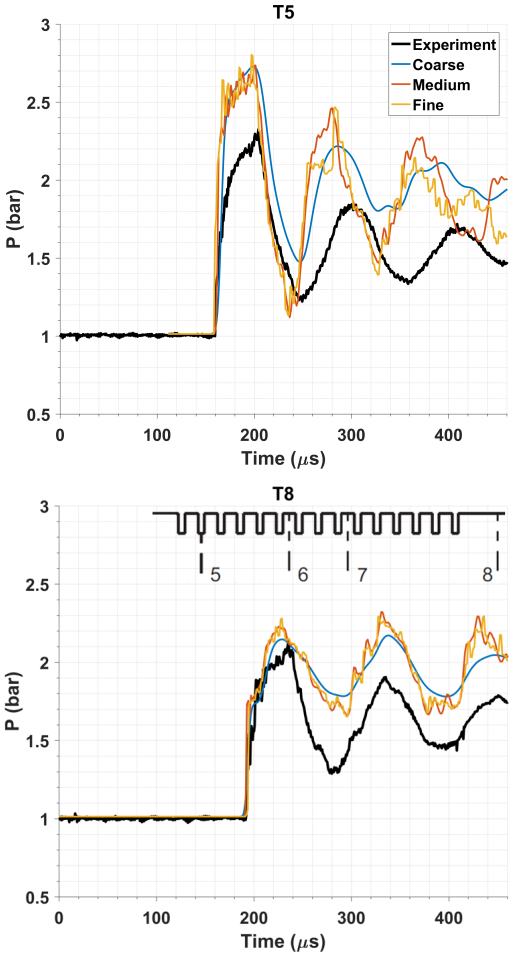

Fig. 9: Inviscid solution pressure history of the single-side grooved duct at two locations for the coarse (blue), medium (red), and fine (orange) unstructured mesh.

Similarly, for the other probes, while the valleys of pressure variation are captured fairly accurately, the peaks are overpredicted by the inviscid simulation. The discrepancies with the experiment are due to a number of reasons. Firstly, the simulated results are inviscid while it was shown that effects of viscosity become important even at early stages of shock diffraction. Secondly, the simulation is two-dimensional while the experiment is conducted in a three-dimensional rectangular duct. Nevertheless, a three-dimensional inviscid simulation is not necessary because it cannot bring up the three-dimensional effects encountered in the physical experiment. Lastly and most importantly, the effect of the evolving boundary layer behind the moving shock cannot be accounted for in the inviscid simulation. It has been assumed that the shock enters the test section without taking into account the effect of viscosity, pressure losses in the long duct preceding the test section, and complex three-dimensional near wall flow development, that are present in the experiment. The shock in the experiment has travelled a total distance of 1750 mm from the diaphragm before entering the test section which is only 130 mm long.

Once the flow is assumed inviscid the duct segment before the test section has no effect and three-dimensional effects in the square duct cannot be taken into account. The previous tests however convincingly demonstrate that viscous flow effects are important for the development of the flow field near the wall and in the grooves especially at the later stages after several passages of the shock over the grooves. It appears that the wave patterns in the core of the duct are little affected by viscous and three-dimensional flow effects, and when a reasonably high mesh resolution is used, are in good agreement with the experimental schlieren. The discrepancies observed in the comparison of the pressure histories of Fig. 9 are further investigated using viscous flow computations.

5 Experiments and Comparisons with Simulation Results

To overcome the shortcomings of the inviscid flow assumption, and identify the effect of the reduced domain size and the initial conditions used, a series of viscous flow simulations for the one-sided grooved duct was carried out. Comparisons with the measured pressure time histories guided the identification of shortcomings in the computations. First, in order to have a better representation of the pressure losses of the flow behind the shock as it travels from the diaphragm to the test section through length of 1750 mm, a two-dimensional channel-like shock tube has been simulated. Next, the 100 mm nozzle extension after the test section was added to the computational domain as existed in the experiment.

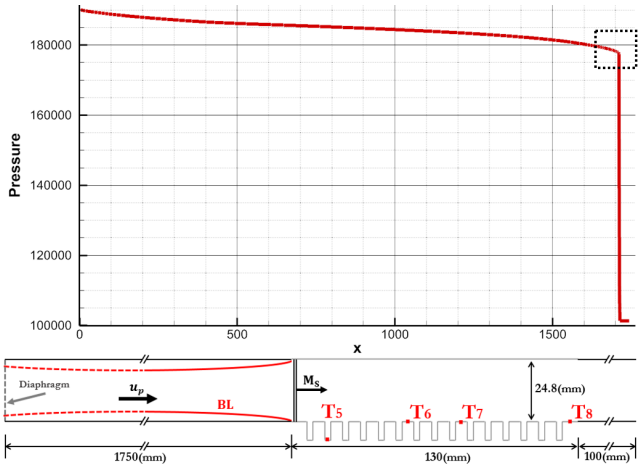

Fig. 10: Computed pressure drop in the channel and schematic of the inflow section with the evolving near-wall flow shape and the computational domains including the test section and the nozzle extension.

A relatively coarse mesh was used with sufficient clustering in the near wall region, capable of capturing the near wall developing flow behind the moving shock and the moving shock itself. The diffusion speed of the boundary layer-type flow developing behind the shock is proportional to the normal component of velocity of the boundary layer, which is significantly smaller compared to the streamwise velocity component (u_{p} of the gas behind the shock). It should also be emphasized that the streamwise spacing for the long tube was not as small as in the case of the test section alone shown previously, however, the mesh size in the streamwise direction was sufficiently fine to capture the shock within acceptable resolution. The high pressure behind the shock determines the strength of the shock (M_{S}). Once the shock travels 1750 mm from the diaphragm and arrives to the test section, the pressure behind it is recorded and is used in conjunction with other flow properties (temperature, density, and mass flow speed u_{p}) for the rest of the computations as inflow for the reduced domain including only the 100 mm long test section.

The plot of the expected pressure drop (in units of Pa) for viscous flow along the tube is shown in Fig. 10. This allows for a better representation of the experiment, taking into account the effect of pressure losses which are estimated to be about 5% and it is representative of the pressure losses in the square duct. Note that the long section of 1750 mm was used in the experiment in order to ensure that the contact discontinuity and the reflected expansion waves do not enter the test section during the time that pressure measurements were taken in the test section.

Table 2: Detailed simulation cases

Case	Description	Grid Resolution
1	Inviscid	14.6 million
2	Viscous (Laminar)	14.6 million
3	Turbulent (SA)	14.6 million
4	Turbulent (SA) inlet profile defined	14.6 million
5	Turbulent (SA) reduced inlet velocity	14.6 million
6	Turbulent (SA) 3D	31.4 million

The inclusion of the upstream section was performed for the 1750 mm long inlet section using a coarse mesh in the stream wise direction to demonstrate the pressure drop (see Fig. 10). Note that the size of the computational mesh would have become very large, if the same grid density required for crisp resolution of the shock in the 230 mm (130 + 100) test section, had been used in the 1750 mm inlet section. In other words, an approximately 110 million cells are required to simulate the inlet section for two-dimensional computations. The inclusion of the boundary layer and reduction of inlet velocity based on the separate computation for the 1750 mm inlet section only on the coarse mesh suggested the reduction of the inlet velocity that improves the agreement with the pressure measurements as shown in Fig. 11. However, the corrections do not affect the shock patterns and the agreement between the computation and the experiment is good as it was shown in Fig. 8.

In order to have a better understanding of the initial conditions that approximate the flow in the experimental test section, five different cases are run on a high-resolution (14.6 million cells) two-dimensional grid. For all cases sufficient stretching near the wall existed to obtain two to three cells for $y^+ < 5$ in order to ensure adequate resolution of turbulent flow. Additionally, in order to take into account the three-dimensional characteristics of the problem, a three-dimensional simulation on a relatively coarse grid with larger cell size, containing 31.4 million cells, has also been conducted. The six cases are summarized in table 2. Small time steps and large number of sub-iterations were used in order to avoid nonlinear instability due to small y^+ values, and to ensure time accuracy of the URANS simulations.

Both laminar (case 2) and turbulent flow simulations with the Spalart-Allmaras (SA) turbulence model (case 3) were obtained. For case 4, an inlet velocity profile based on a polynomial approximation to the Blasius solution is specified as in the shock diffraction case of Fig. 6 (d). In case 5, the same inlet conditions as case 3 were used, but with a reduced inlet velocity (u_{p}). In the simulation of the full shock tube, it was seen that due to the shape of the evolving near wall layer (observed in two-dimensional simulations but exaggerated in the

schematic of Fig. 10) the velocity of the core flow accelerates in the contraction and then decelerates through the divergent part of the near wall displacement thickness.

Results of pressure history for the six cases are shown in Fig. 11. The comparisons clearly show that the inviscid simulation even with reduced inflow pressure does not correctly predict the pressure history at the pressure probe T_5 and results in premature and overpredicted peak values. Even though the first peak and throat are captured quite well, there is a significant lagging phase error past $t \approx 250$ μs. Also the pressure peaks are not decreasing as they should due to the viscous effects. The computed results generally improve for viscous flows, and case 5 (turbulent with the SA model and reduced inlet velocity) matches the experiment quite well at the first pressure probe T_5 at all times. Overall, it appears that case 3: Turbulent flow simulation with the SA model performs the best in average for all the probes T_5, T_6, T_7, and T_8, with the exception of slightly overestimating the second and third peaks at the pressure probe T_5 by approximately 10% and 20%, respectively. It also appears that the discrepancies at peak pressures at about $t = 300$ μs and $t = 400$ μs are not due to three-dimensional effects.

A two-dimensional simulation (not shown here) with identical streamwise (x, y) centerline section of the three-dimensional grid demonstrated that the time variation of the pressure is virtually the same with the pressure variation of the mid-plane of the full 3D simulation. This indicates that the 3D effects do not affect the variation of pressure at the pressure probe locations significantly. Links to animations are also provided in the caption of Fig. 11 which illustrate the numerical schlieren results side by side with pressure history at the pressure probes T_5, T_6, T_7, and T_8 in order to better understand the relation between the measured, the computed pressure, and the simulated flowfield structure in real time.

For the three-dimensional simulation, a comparison of pressure at the start, the middle, and the end of the side wall is shown in Fig. 12. It is clear that the strength of the shock reduces and a reduction in the pressure jump (approximately 17%) as the shock travels from left (T_1) to right (T_3) is obtained. The full duct computation revealed certain three-dimensional characteristics in the flow even when a reduced domain is employed. Eddies can be identified using isosurfaces of Q-criterion [23] defined as the second invariant of the velocity gradient tensor. In Fig. 13, the isosurfaces are coloured by velocity magnitude, while the mid-plane shows numerical schlieren in gray scale at two different times. It is seen that the strongest vortices (shown

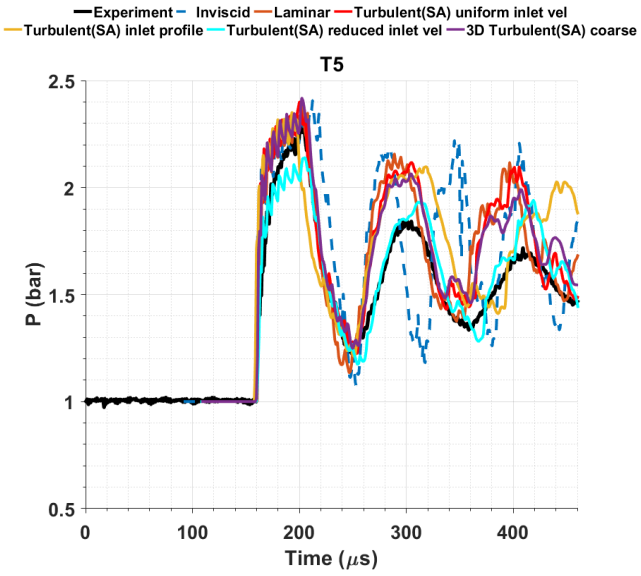

Fig. 11: Pressure history at probe T_5 in the single-sided grooved duct for $P_L/P_R = 4$. T_5 (Online Resource 6). T_6, T_7, and T_8 (Online Resource 7).

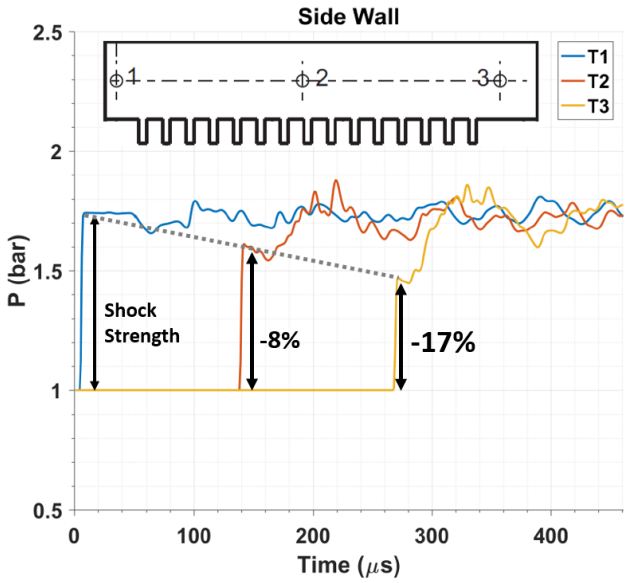

Fig. 12: Time history of pressure on the side wall for the 3D case.

in red colour) are created as the shock diffracts from the grooves immediately behind it. Additionally, three-dimensional corner vortices on each side as the shock passes the grooves is visible. In addition, horseshoe-like vortices can be seen towards the end of the test section at a later time when the shock has moved out of the test section. These features could impact the pressure at the monitored locations given a higher resolution of the computational domain which requires at least several hundred million cells. Furthermore, the current isosur-

faces show little or no impact of the corner vortices on the mid-section ($z = 0$) where the pressures have been recorded in the experiment. The wave patterns of the core, even though not very well resolved, also appear to be little affected by the three-dimensional effects. The current three-dimensional mesh provides sufficient results and is comparable to the two-dimensional mesh resolution in the grooves and the near wall region. It is estimated however that in order to reach the same uniform level of resolution as the two-dimensional cases in the core region, over one billion cells will be needed.

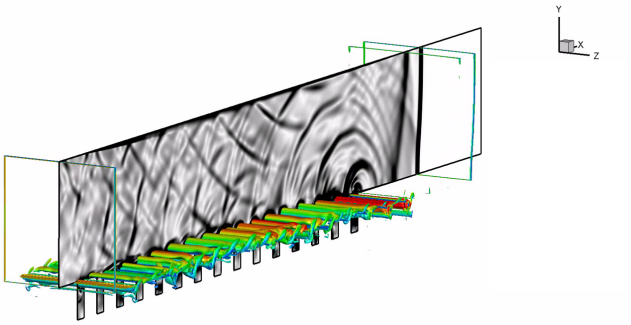

(a) $t = 280$ μs

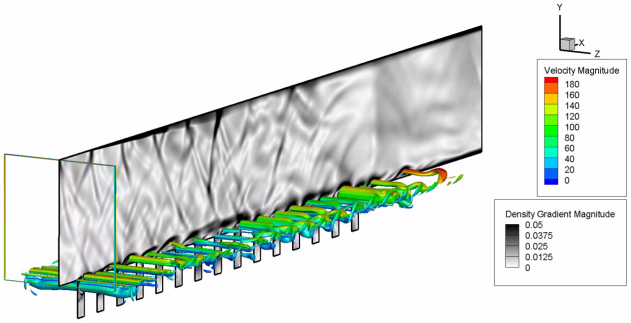

(b) $t = 440$ μs

Fig. 13: Isosurfaces of Q-criterion coloured by velocity magnitude at two different times.

The three-dimensional results shown of Fig. 13 have been obtained on a much coarser mesh (only the near wall resolution remained almost the same as in the two-dimensional case in order to properly resolve viscous flow effects). Furthermore, a shorter domain that did not include the 100 mm extension of the attenuation section was used in order to reduce the total mesh size. We agree that spurious reflections from the truncated outflow appear at $t = 440$ μs but we only included Fig. 13 to demonstrate that blockage and three dimensional effects in the near wall region become more prominent at the downstream sections.

The numerical schlieren for the viscous computation for the single-sided and double-sided grooved duct was in agreement with the experiment as the inviscid computation of Fig. 8. A comparison of the two-dimensional (SA) computed pressure for the double-side grooved duct at the four specified pressure probes is shown in Fig. 14. The peaks at the pressure probe T_5 are not predicted very well after $t = 250$ μs with an $\text{error}_{\max} \approx 20\%$. The rest of the results are in agreement with the experiment for the pressure probes T_6, T_7, and T_8. The main features of the flow are correctly predicted for all pressure probe locations as long as the thick flow wall layer in the long driven section of the shock tube has not entered the test section, and while the shock remains in the test section. The predictions for the pressure probe T_6 show good agreement with the experiment especially after $t = 220$ μs. The pressure probe T_7 also shows good agreement until around $t = 380$ μs. The agreement at the pressure probe T_8 is lost around $t = 320$ μs and reaches an $\text{error}_{max} \approx 15\%$.

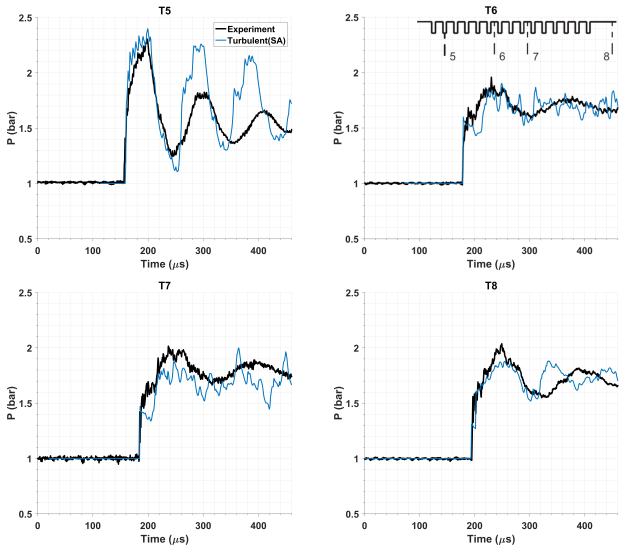

Fig. 14: Time history of pressure for the double-sided grooved duct with $P_{\text{L}}/P_{\text{R}} = 4$.

A comparison between experimental and numerical results for the propagation speed (W_{S}) of the incident shock wave in one-sided and double-sided grooves along with the secondary shock speed for $P_{\text{L}}/P_{\text{R}} = 4$ are shown in Fig. 15. As in the experiment, the numerical data are recorded for the same number of snapshots in time, measuring the travelled distance in each time segment and calculating the shock speed by: $W_{\text{S}} = \frac{(x_{n+1}-x_n)}{(t_{n+1}-t_n)}$, where n represents the snapshot number. The numerical results are in very good agreement with

the experimental measurements. The velocity decreases almost linearly after the first interaction of the propagating shock with the grooves at $t = 20$ μs. It can be seen that the shock speeds are significantly lower in the case of double-sided grooves. This supports the hypothesis that grooves on all sides of a duct will further reduce the strength of the shock. In addition, the secondary shock starts forming around $t = 230$ μs and accelerates until it catches up with the primary moving shock.

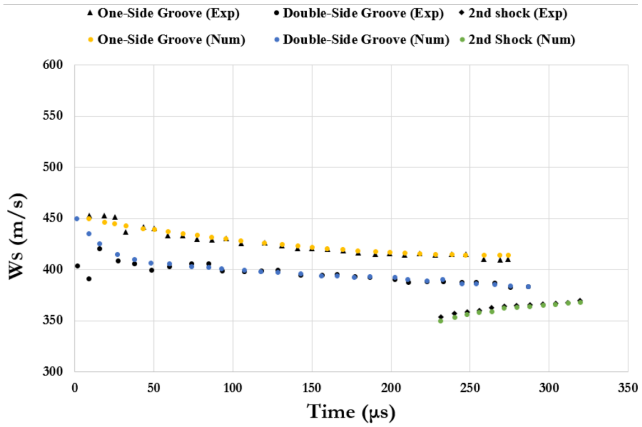

Fig. 15: Experimental and numerical comparison of shock speed propagation (W_S) in single-sided and double-sided grooved duct for $P_L/P_R = 4$.

5.1 Pressure Ratio Effect

A higher diaphragm pressure ratio $P_L/P_R = 12$ has been simulated to compare with the experiment and to understand the effect of shock strength on propagation speed and attenuation of the moving shock. Using Eq. 1, the theoretical Mach number of the moving shock corresponding to this pressure ratio is found to be: $M_S = 1.66$. The flow properties behind and after the shock are obtained from unsteady moving shock equations [24] as summarized in Table 1. Comparison of experimental and numerical schlieren of the viscous flow simulations for the single-sided grooved duct with $P_L/P_R = 12$ are shown in Fig. 16, and the results are in good agreement with the experiment as in the lower pressure ratio case. Time histories of the computed pressure are compared against the experimental recordings in Fig. 17. Even though the main features are captured in the computation it appears that the peaks at the pressure probes T_5 and T_8 are not correctly predicted after $t = 250$ μs and $t = 180$ μs respectively. Compared to the single-sided grooves at lower pressure ratio ($P_L/P_R = 4$) case, clearly, the peaks are higher for the stronger shock while the pressure trends more or less stay the same.

Numerical schlieren of the viscous simulations and higher pressure ratio $P_L/P_R = 12$ for the double-sided grooved duct only are presented in Fig. 18. The results could not be compared against the experiment since the experimental schlieren images were not recorded for this particular case. However, the comparison between the pressure history for the double-sided grooved duct and the available experimental measurements shown in Fig. 19 demonstrates quite good agreement with the experiment. The peaks and valleys at pressure probe T_5 are correctly predicted. The pressure variations are in agreement with the experiment for the pressure probe T_8, and the main features of the flow are captured. Compared to the single-sided grooves, the pressure fluctuations diminish faster in the double-sided grooves as seen at the pressure probe T_8 for example. Clearly, in comparisons for time larger than $t = 420$ μs the shock has exited the test section, yet the comparison of the computed pressure with the measurements is quite favourable.

The comparison between experimental and numerical propagation speed (W_S) of the moving shock in single-sided and double-sided grooves along with the secondary shock speed for $P_L/P_R = 12$ are shown in Fig. 20. The computed speeds agree with those obtained from the experiment. The velocity decreases almost linearly after $t = 20$ μs. Steeper velocity decrease can be seen in the case of double-sided grooves, and the formation of secondary shock wave occurs earlier in time and accelerates faster compared to the lower pressure ratio case ($P_L/P_R = 4$). More importantly, it is found that for stronger shocks, the slope of the decrease is steeper compared to weaker shocks, and this is important as it shows that grooves are more effective in attenuating the shock of higher strength.

5.2 Groove Geometry Effects

Different groove geometries have been tested in the numerical simulations only in order to identify and better understand the contribution of groove geometry to pressure attenuation in the double-sided grooved duct. The initial and boundary conditions are kept the same while the geometry of the groove is modified in an attempt to reduce the intensity of the shock. Numerical schlieren for four groove shapes at two different time steps of $t = 220$ μs (the shock reaches the end of the grooves), and $t = 570$ μs (the shock reaches the end of the domain) are shown in Fig. 21. At $t = 220$ μs, the secondary shock is catching up with the primary

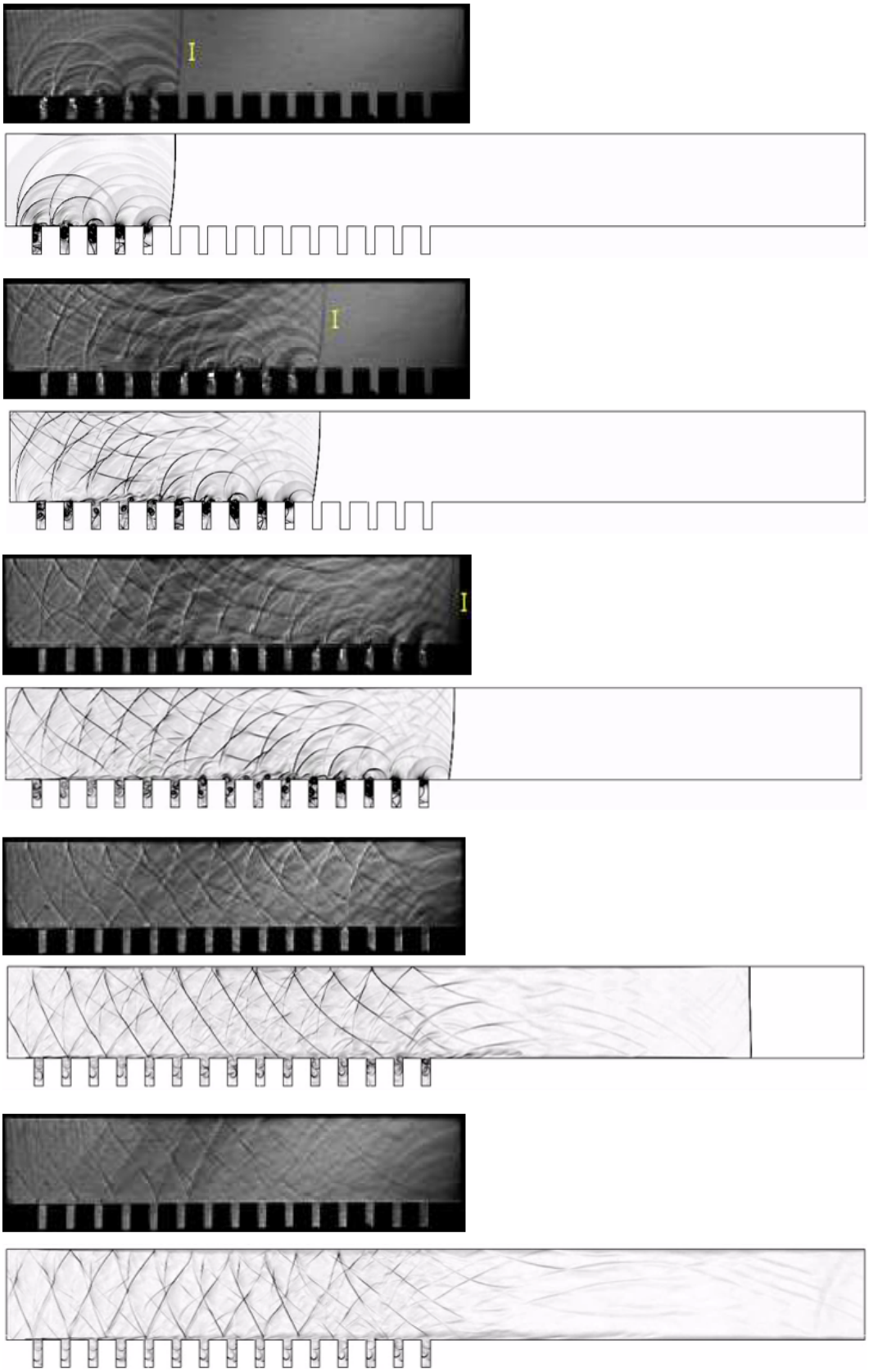

Fig. 16: Comparison of experiment and computation for shock propagation of strength $P_{\mathrm{L}}/P_{\mathrm{R}} = 12$ in single-side grooved duct at $92, 172, 252, 404, 660$ μs. Top: Experimental Schlieren, Bottom: Numerical Schlieren.

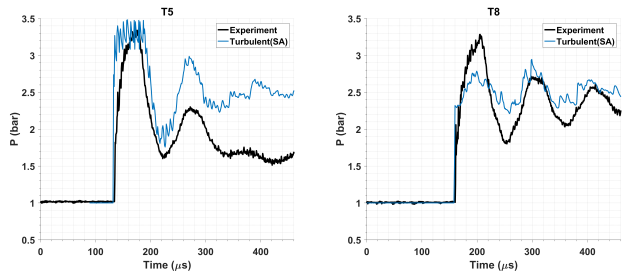

Fig. 17: Time history of pressure for the single-side grooves with $P_{\mathrm{L}}/P_{\mathrm{R}} = 12$.

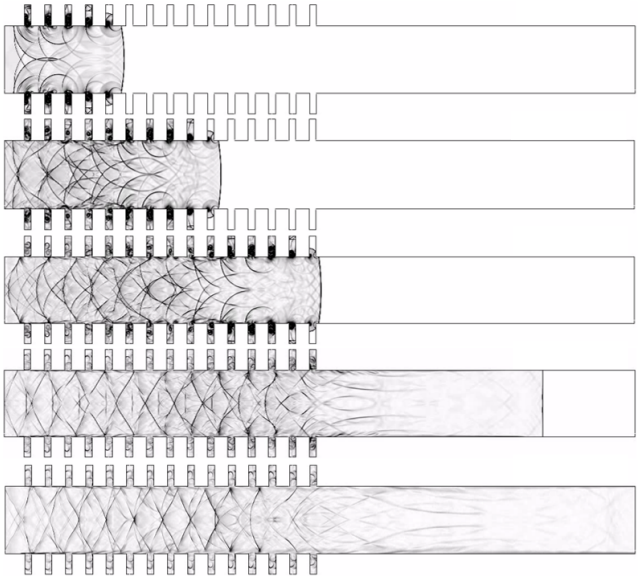

Fig. 18: Numerical Schlieren for shock propagation of strength $P_{\mathrm{L}}/P_{\mathrm{R}} = 12$ in double-sided grooved duct at $92, 172, 252, 404, 660$ μs.

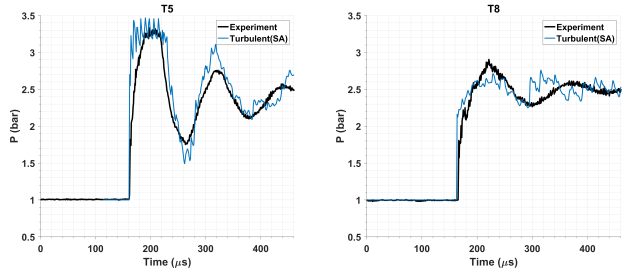

Fig. 19: Time history of pressure for the double-sided grooves with $P_{\mathrm{L}}/P_{\mathrm{R}} = 12$.

moving shock the fastest for the v-shape grooves and slowest for the backward tilted grooves. This accelerates the shock front as it can be seen at $t = 570$ μs which shows in the v-shape groove the primary moving shock is traveling the fastest reaching the end line first. A third weak shock is also formed in all the cases except

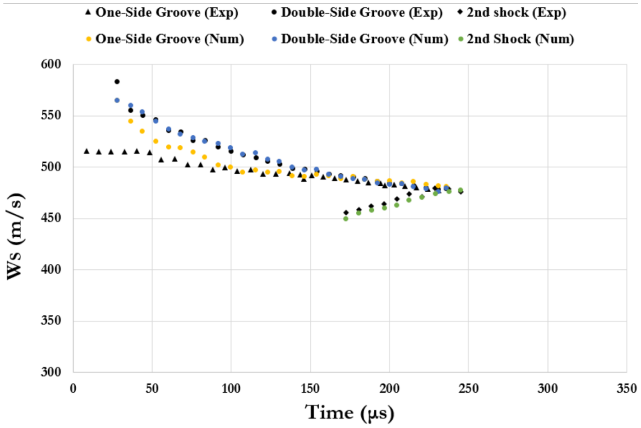

Fig. 20: Experimental and numerical comparison of shock speed propagation (W_{S}) for $P_{\mathrm{L}}/P_{\mathrm{R}} = 12$.

for the last, and accelerates the most in the v-shape grooves.

Strongest reflections from grooves are seen in the round edge grooves which explain the largest deceleration of the shock front. Overall, fewer disturbances in the flow field behind the primary shock develop in the backward tilted case. For different groove shapes however, comparisons for the computed results demonstrate that the backward tilted grooves exhibit the lowest pressure variation while the rounded grooves show the highest peaks at the final time $t = 570$ μs. For different groove shapes, the same trends observed for the standard rectangular grooves carry over.

5.3 Shock Propagation in Branched Ducts with 90° Junction

Both in the experiment and in the numerical simulations, the shock waves transmitted down a 90° branch, are found to be significantly weaker than those propagating along a single direction, which is in agreement with previous experimental investigation [25]. Numerical schlieren are compared against the experiment for the single- and double-sided grooves in Figs. 22 and 23, respectively at two different times. In order to find out whether the sharp variations shown in Fig. 22 (right), both in the experiment and the simulation, are shocks or strong pressure waves, entropy plots were produced in the simulations, and it was found that the variations shown in these figures are strong pressure waves and not moving shocks since no entropy jump was seen.

Time history of pressure for single- and double-sided grooves at four locations, are plotted in Figs. 24 and 25, respectively. For the single-sided grooves, at pressure probes T_5, T_6, and T_7 the agreement between ex-

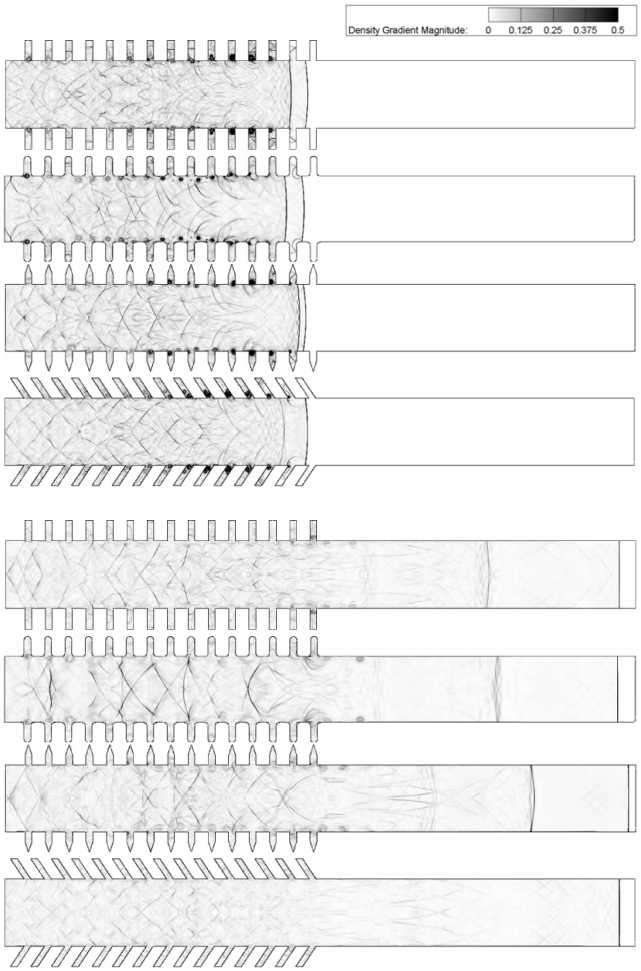

Fig. 21: Numerical Schlieren of the four different groove shapes for $P_L/P_R = 4$ at (Top) $t = 180$ μs, and (Bottom) $t = 440$ μs.

periment and computation is lost after $t \approx 250$ μs. The pressure at all locations begin to match after $t \approx 400$ μs. Closest agreement is seen at the pressure probe T_9 in Fig. 24 where the diffracted weak shock has just passed the T_9 pressure probe. As in the straight duct case, this disagreement is attributed to the non-uniform flow that exists in the long duct of the experiment. In addition, the smaller jump at pressure probe T_9 compared to the pressure probe T_7 verifies the significant weakening of the shock propagating down the 90° branch as it was also found in the previous experimental investigations [25].

For the double-sided grooves, however, Fig. 25 demonstrates better agreement at the pressure probes T_5, T_6, and T_7 with an error $\approx 20\%$ at pressure probe T_5 at $t \approx 350$ μs . At pressure probe T_9 the agreement is lost after $t \approx 380$ μs. Better agreement is seen at pressure probe T_7 with an error $\approx 5\%$. This is consistent with the results of single- and double-sided grooves for the straight duct found in Figs. 17 and 19 for the higher pressure ($P_L/P_R = 12$). It appears that in the case of double-sided grooves (see Fig. 19 for example), the effects of the near wall flow in the upper wall are diminished and the agreement of the simulation with the measurements improves.

The comparison between experimental and numerical results for the propagation speed (W_S) of the incident shock wave in single- and double-sided grooves 90° branched duct along with the secondary shock speed for $P_4/P_1 = 4$ are shown in Fig. 26. The computed propagation speeds are in agreement with those obtained in the experiment between $t = 50$ μs and $t = 180$ μs. The velocity decreases almost linearly after $t = 60$ μs. Slightly lower velocities can be seen in the case of double-sided grooves, and the formation of the secondary shock wave occurs around the same time ($t = 240$ μs) as in the straight duct. Furthermore, the secondary shock seems to accelerate at a lower rate compared to that of the experiment. Experimental results do not exist past $t = 160$ μs however, computed results are plotted for illustration of the speed evolution as the shock propagates downstream. A higher diaphragm pressure ratio of: $P_L/P_R = 12$ has been simulated numerically for the single-sided 90° branch angle to compare with experiment. The theoretical Mach number of the moving shock is found through Eq. 1 to be: $M_S = 1.66$. Note the shock speeds in Figs. 15, 20, and 26 were measured with pressure gauges. The flow properties behind and after the shock are the same as those of the 0° straight duct. Numerical schlieren of the viscous simulations for this case is compared against the experiment. The results are qualitatively in good agreement with experiment at several times as shown in Fig. 27. At later stages of time, interaction between the vortex roll-off from the branched duct (similar to the diffraction test case in Fig. 6) with a reflected wave traveling upstream is seen. It was verified that these regions are strong pressure waves and not shock waves as no entropy jump was seen. For this case, there were no recorded pressures to compare.

Additional experimental results for different branching angles have been shown in Fig. 4. The corresponding propagation speed and pressures indicate that the single-sided groove configuration presents the greatest deceleration of the shock at angles smaller than 90°. A 9.3% deceleration is obtained with the straight duct for a pressure ratio of $P_L/P_R = 4$. In addition, the single-sided groove configuration with a 45° junction is more effective in reducing the pressure by 27.7% for $P_L/P_R = 4$. A 24.6% attenuation is achieved with $P_L/P_R = 12$ in the 120° junction. For the $P_L/P_R = 8$ a reduction of 20% is attained for a 30° junction with double-side

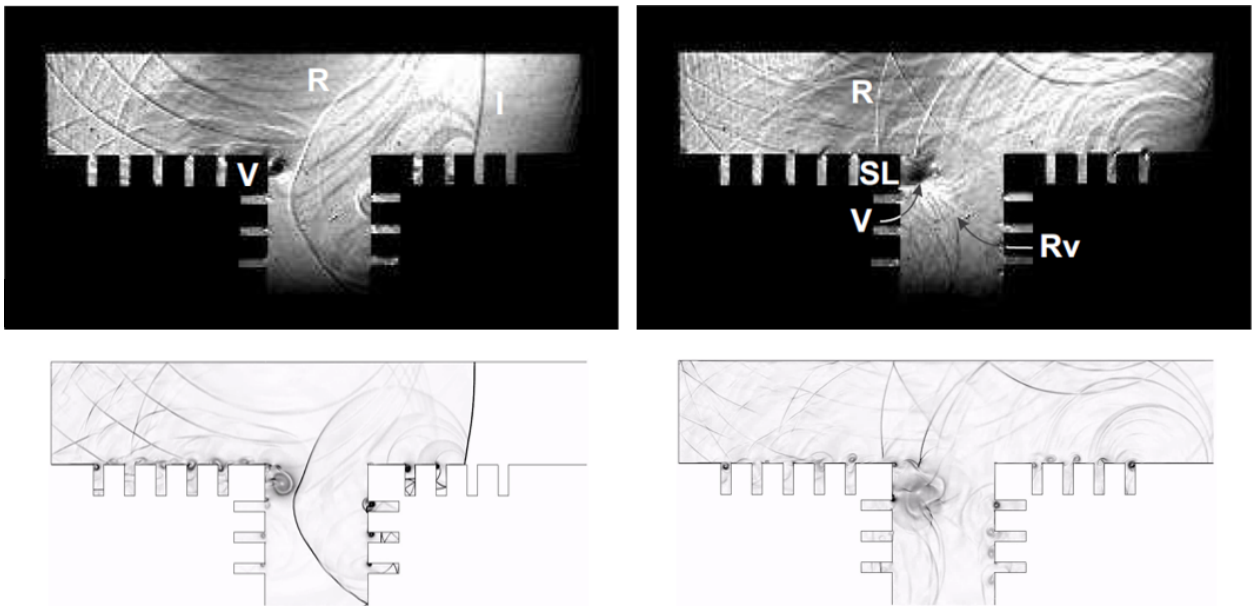

Fig. 22: Comparison of shock propagation in single-sided groove 90° branched duct at $t = 347$ μs and $t = 442$ μs for $P_{\mathrm{L}}/P_{\mathrm{R}} = 4$. (Top): experiment, (Bottom): computation.

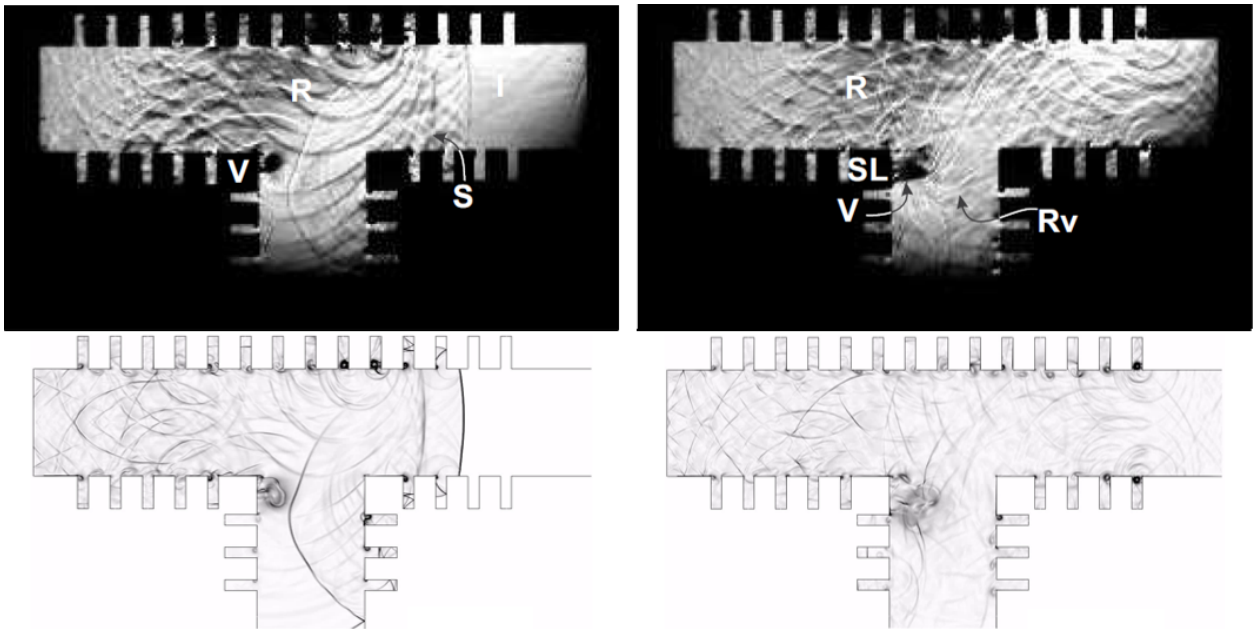

Fig. 23: Comparison of shock propagation in double-sided groove 90° branched duct at $t = 347$ μs and $t = 442$ μs for $P_{\mathrm{L}}/P_{\mathrm{R}} = 4$. (Top): experiment, (Bottom): computation.

grooved walls. Furthermore, the double-sided groove configuration was found to suppress the fluctuating pressures more efficiently. It appears that duct branching has a favourable effect, however in many cases is not possible (for example in high-speed train tunnels) therefore the alterations of the groove geometry (see Fig. 21) may be a more effective alternative in reducing shock strength.

6 Conclusions

Overall, good agreement between high-resolution two-dimensional computations and the experiment has been obtained for the shock speeds and complex wave patterns created by the grooves. Even inviscid flow simulations were in reasonable agreement with experimental schlieren images, however accurate surface pressure

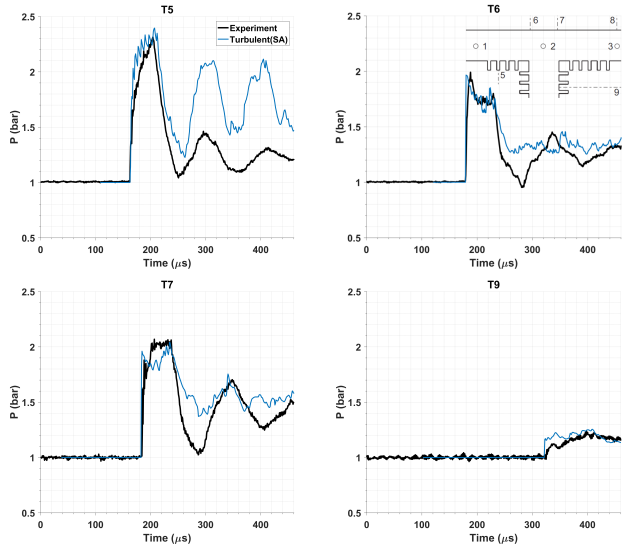

Fig. 24: Time history of pressure for the 90° single-sided groove branched duct with $P_{\mathrm{L}}/P_{\mathrm{R}} = 4$.

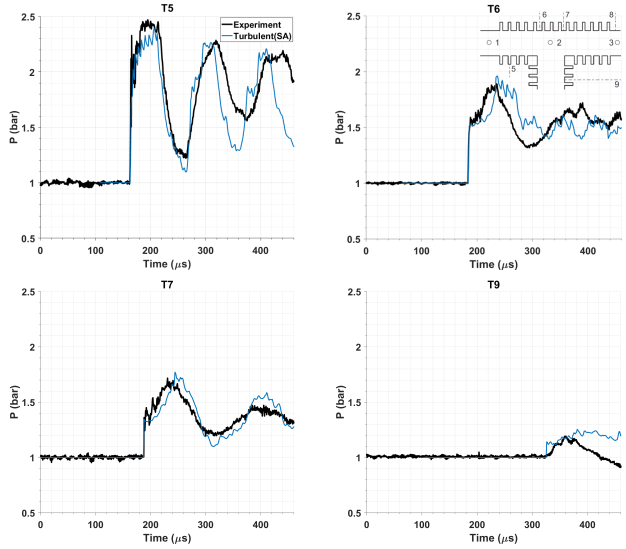

Fig. 25: Time history of pressure for the 90° double-sided groove branched duct with $P_{\mathrm{L}}/P_{\mathrm{R}} = 4$.

prediction in long ducts with grooves requires use of URANS to account for the near wall viscous flow effects, and pressure losses associated with the moving shock. It is found that accurate pressure history predictions require a complete representation of the full experimental setup to allow full capturing of the flow development, and pressure losses associated with the unsteady flow and the moving shocks in long rectangular ducts. The main features of the variation of pressure at different pressure probe locations, however can be obtained from the two-dimensional simulations of the flow domain. The experimental and numerical findings suggest that effective attenuation of shocks propagating in ducts can be achieved when roughness in the form of grooves are incorporated. As expected, double-sided grooved walls are more effective than single-sided groove in terms of reducing the speed of the shock front (W_{S}), hence the strength (M_{S}), and the pressure jump across it. Numerical simulations indicated that the effect of the groove shape is also significant on shock attenuation.

Acknowledgements The authors wish to acknowledge the Vega high performance cluster at ERAU for providing the computational resources to perform the simulation reported in the present paper. We would also like to acknowledge Nalleli Gongora-Orozco for the help and support during the experiment and the technical staff at the University of Manchester for manufacturing the required parts for the shock tube.

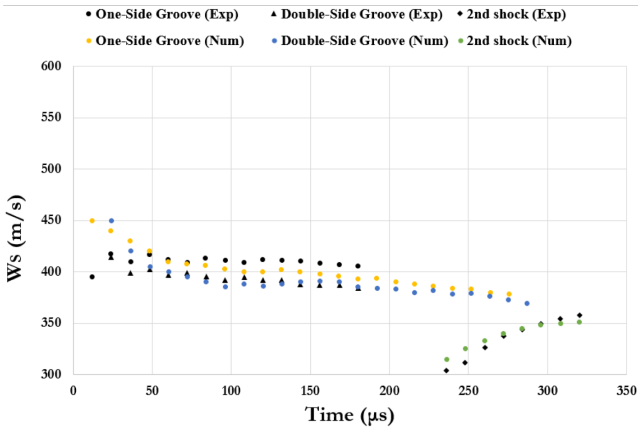

Fig. 26: Experimental and numerical comparison of shock speed propagation (W_{S}) in 90° branched duct for $P_{\mathrm{L}}/P_{\mathrm{R}} = 4$.

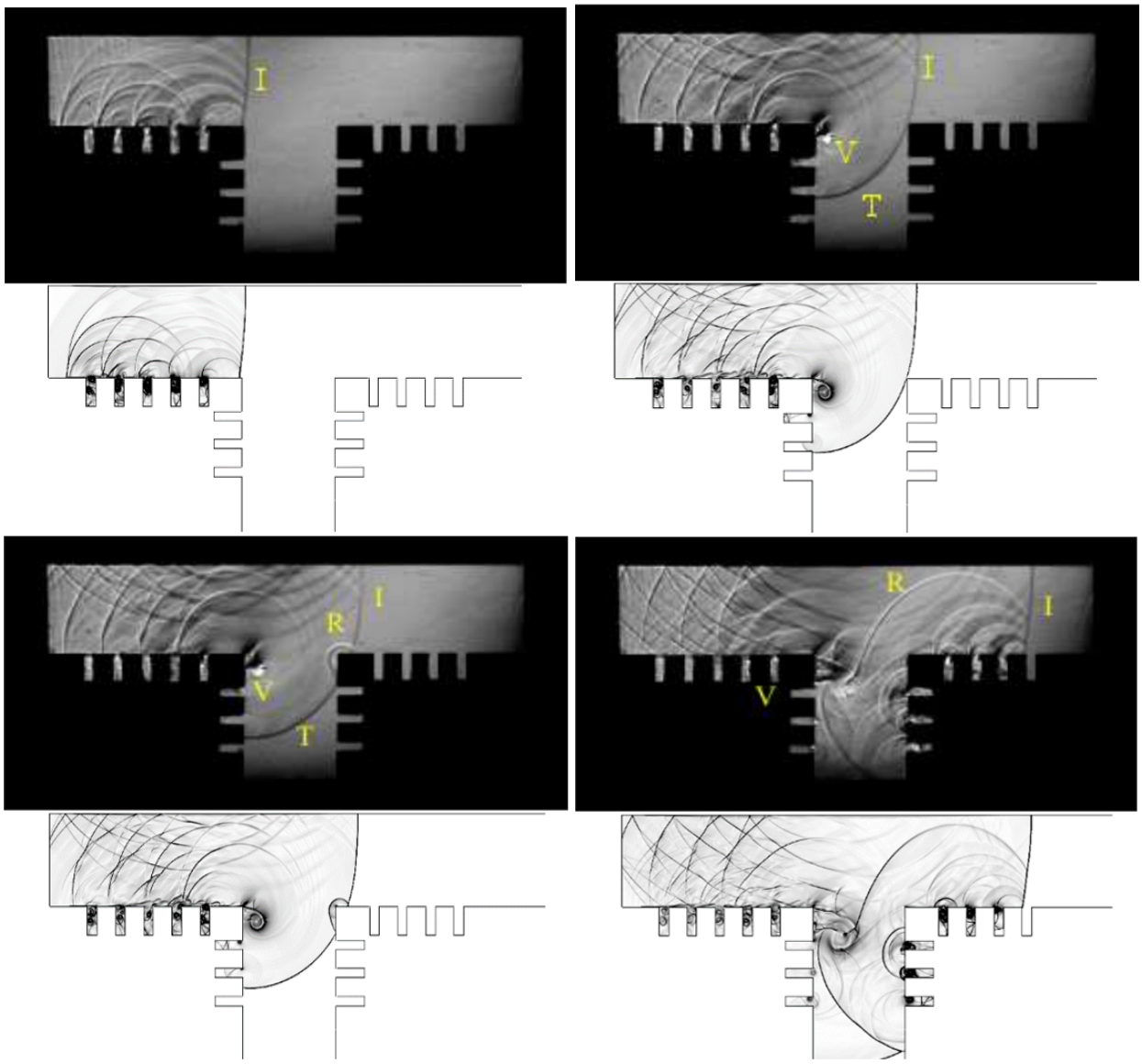

Fig. 27: Comparison of shock propagation in double-sided groove 90° branched duct for $P_{\mathrm{L}}/P_{\mathrm{R}} = 12$ at $105, 175, 182, 240$ μs. (Top): experiment, (Bottom): computation. Experimental images from [13].

References

1. P. Woodward, P. Colella: The numerical simulation of two-dimensional fluid flow with strong shocks. J. Comput. Phys. **54**(1), 115–173 (1984). doi:10.1016/0021-9991(84)90142-6
2. O. Igra, J. Falcovitz, H. Reichenbach, W. Heilig: Experimental and numerical study of the interaction between a planar shock wave and a square cavity. J. Fluid Mech. **313**, 105–130 (1996). doi:10.1017/S0022112096002145
3. M. Sun, K. Takayama: The formation of a secondary shock wave behind a shock wave diffracting at a convex corner. Shock Waves **7**(5), 287–295 (1997). doi:10.1007/s001930050083
4. O. Igra, X. Wu, J. Falcovitz, T. Meguro, K. Takayama, W. Heilig: Experimental and theoretical study of shock wave propagation through double-bend ducts. J. Fluid Mech. **437**, 255–282 (2001). doi:10.1017/S0022112001004098
5. M. Sun, K. Takayama: Vorticity production in shock diffraction. J. Fluid Mech. **478**, 237–256 (2003). doi:10.1017/S0022112002003403
6. A. Britan, A. Karpov, E. Vasilev, O. Igra, G. Ben-Dor, E. Shapiro: Experimental and numerical study of shock wave interaction with perforated plates. Journal of Fluids Engineering **126**(3), 399–409 (2004). doi:10.1115/1.1758264
7. H. Hornung, J. Taylor: Transition from regular to mach reflection of shock waves part 1. the effect of viscosity in the pseudosteady case. J. Fluid Mech. **123**, 143–153 (1982). doi:10.1017/S0022112082002997
8. S. Jin, J.G. Liu: The effects of numerical viscosities: I. slowly moving shocks. J. Comput. Phys. **126**(2), 373–389 (1996). doi:10.1006/jcph.1996.0144
9. M. Sun, T. Ogawa, K. Takayama: Shock propagation in narrow channels. ISSW23, Fort Worth, TX (2001)
10. S. Pirozzoli, F. Grasso: Direct numerical simulation of impinging shock wave/turbulent boundary layer interaction at M= 2.25. Physics of Fluids **18**(6), 065,113 (2006). doi:10.1063/1.2216989
11. M. Movahed, H. Groenig: Pressure wave damping in branched pipes with arbitrary angles. International Journal of Pressure Vessels and Piping **23**(3), 215–225 (1986). doi:10.1016/0308-0161(86)90020-7
12. N. Gongora Orozco, Experimental studies on internal shock wave phenomena and interactions. Ph.D. thesis, University of Manchester (2010)
13. N. Gongora-Orozco, H. Zare-Behtash, K. Kontis: Experimental studies on shock wave propagating through junction with grooves (2009). doi:10.2514/6.2009-327
14. A.G. Gaydon, I.R. Hurle, *The Shock Tube in High-Temperature Chemical Physics* (Chapman and Hall, 1963)
15. F. Palacios, J. Alonso, K. Duraisamy, M. Colonno, J. Hicken, A. Aranake, A. Campos, S. Copeland, T. Economon, A. Lonkar, et al.: Stanford university unstructured (su2): an open-source integrated computational environstment for multi-physics simulation and design (2013). doi:10.2514/6.2013-287
16. E.F. Toro, *Riemann Solvers and Numerical Methods for Fluid Dynamics: A Practical Introduction* (Springer Science & Business Media, 2013)
17. S. Zhang, Y.T. Zhang, C.W. Shu: Interaction of an oblique shock wave with a pair of parallel vortices: Shock dynamics and mechanism of sound generation. Physics of Fluids **18**(12), 126,101 (2006). doi:10.1063/1.2391806
18. K.T. Panourgias, J.A. Ekaterinaris: A discontinuous galerkin approach for high-resolution simulations of three-dimensional flows. Computer Methods in Applied Mechanics and Engineering **299**, 245–282 (2016). doi:10.1016/j.cma.2015.10.016
19. K.T. Panourgias, J.A. Ekaterinaris: A nonlinear filter for high order discontinuous galerkin discretizations with discontinuity resolution within the cell. J. Comput. Phys. **326**, 234–257 (2016). doi:10.1016/j.jcp.2016.08.049
20. B.W. Skews: The perturbed region behind a diffracting shock wave. J. Fluid Mech. **29**(4), 705–719 (1967). doi:10.1017/S0022112067001132
21. T. Bazhenova, L. Gvozdeva, V. Komarov, B. Sukhov: Diffraction of strong shock waves by convex corners. Fluid Dynamics **8**(4), 611–619 (1973). doi:10.1007/BF01013100
22. H. Onodera, K. Takayama: Interaction of a plane shock wave with slitted wedges. Experiments in Fluids **10**(2-3), 109–115 (1990). doi:10.1007/BF00215018
23. J. Jeong, F. Hussain: On the identification of a vortex. J. Fluid Mech. **285**, 69–94 (1995). doi:10.1017/S0022112095000462
24. J.D. Anderson, *Modern Compressible Flow: With Historical Perspective*, vol. 12 (McGraw-Hill New York, 1990)
25. O. Igra, L. Wang, J. Falcovitz, W. Heilig: Shock wave propagation in a branched duct. Shock Waves **8**(6), 375–381 (1998). doi:10.1007/s0019300501